Supplementary Information for
"Electronic and magnetic excitations in La$_3$Ni$_2$O$_7$"

Xiaoyang Chen,[1, *] Jaewon Choi,[2, *] Zhicheng Jiang,[3] Jiong Mei,[4, 5] Kun Jiang,[4, 5] Jie Li,[6]

Stefano Agrestini,[2] Mirian Garcia-Fernandez,[2] Hualei Sun,[7] Xing Huang,[8] Dawei Shen,[3]

Meng Wang,[8] Jiangping Hu,[4, 9] Yi Lu,[6, 10, †] Ke-Jin Zhou,[2, ‡] and Donglai Feng[3, 11, 10, §]

[1]*State Key Laboratory of Surface Physics, Department of Physics,*
and Advanced Materials Laboratory, Fudan University, Shanghai 200438, China
[2]*Diamond Light Source, Harwell Campus, Didcot OX11 0DE, UK*
[3]*National Synchrotron Radiation Laboratory and School of Nuclear Science and Technology,*
University of Science and Technology of China, Hefei, 230026, China
[4]*Beijing National Laboratory for Condensed Matter Physics and Institute of Physics, Chinese Academy of Sciences, Beijing 100190, China*
[5]*School of Physical Sciences, University of Chinese Academy of Sciences, Beijing 100190, China*
[6]*National Laboratory of Solid State Microstructures and Department of Physics, Nanjing University, Nanjing 210093, China*
[7]*School of Science, Sun Yat-Sen University, Shenzhen, Guangdong 518107, China*
[8]*Guangdong Provincial Key Laboratory of Magnetoelectric Physics and Devices,*
School of Physics, Sun Yat-Sen University, Guangzhou, Guangdong 510275, China
[9]*New Cornerstone Science Laboratory, Beijing, 100190, China*
[10]*Collaborative Innovation Center of Advanced Microstructures, Nanjing, 210093, China*
[11]*New Cornerstone Science Laboratory, University of Science and Technology of China, Hefei, 230026, China*
(Dated: October 19, 2024)

Supplementary Note 1. Material.

Figure S1(a) shows the X-ray diffraction (XRD) result of the single crystal La$_3$Ni$_2$O$_7$ using Cu-K_α X-rays (λ = 1.54 Å). XAS and RIXS experiments were conducted on the very sample. All diffraction peaks correspond to the lattice constant $c \sim 20.5$ Å and no extra peaks appear, indicating negligible oxygen vacancies therein. Figure S1(b) illustrates the Laue pattern taken for the same sample. As shown in Fig. S1(b), the sharp X-ray Laue pattern taken from the same sample further confirms its well-defined (001) crystalline cleavage plane and high quality.
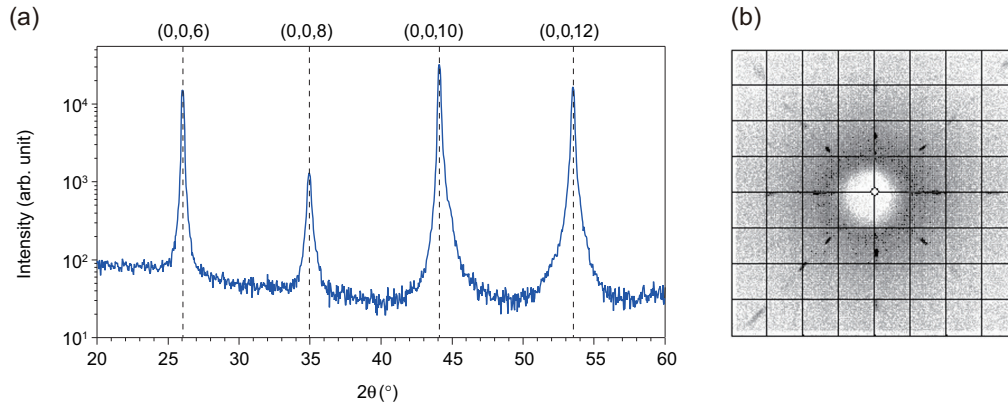

FIG. S1. (a) X-ray diffraction on the La$_3$Ni$_2$O$_7$ sample measured in RIXS experiments. (b) X-ray Laue pattern taken on the (001) cleavage plane of the very La$_3$Ni$_2$O$_7$ single crystal.

* Equal contributions
† yilu@nju.edu.cn
‡ kejin.zhou@diamond.ac.uk
§ dlfeng@ustc.edu.cn

Supplementary Note 2. Multiplet calculation.

2.1 Model and parameters.

Model construction. — We construct a fully correlated double-cluster model consisting of the top and bottom corner sharing NiO_6 octahedra in the bilayer structure, which includes all five $3d$ orbitals of each Ni site and all $2p$ orbitals of the eleven surrounding oxygen sites. For the spectroscopic process, additional Ni $2p$ core orbitals are included. To ease future analysis, we combine the oxygen orbitals surrounding each Ni site into symmetry adapted molecular orbitals of tetragonal D_{4h} symmetry. Such a procedure results in two sets of ligand orbitals of z^2, $x^2 - y^2$, xy, xz/yz symmetry, each coupling to their corresponding Ni $3d$ orbitals with the same symmetry. We denote these orbital degrees of freedom by L. The remaining oxygen $2p$ orbitals couple to the Ni $3d$ orbitals only indirectly via the L orbitals and are denoted as L'. With open boundary condition, the Hamiltonian reads

$$H = \sum_{\alpha}(H_d^{\alpha} + H_L^{\alpha} + V_{dL}^{\alpha\alpha}) + \sum_{\alpha,\alpha'\neq\alpha}(V_{dL}^{\alpha\alpha'} + V_{LL}^{\alpha\alpha'}) + H_{LL'}, \tag{S1}$$

where $\alpha \in \{t, b\}$ denotes the top and bottom clusters, respectively. The local terms of the $3d$ sites read

$$H_d^{t,b} = \sum_{ij}\epsilon_d^{ij}d_i^{\dagger}d_j + \sum_{ijkl}U^{ijkl}d_i^{\dagger}d_j^{\dagger}d_ld_k,$$

where $d_i^{(\dagger)}$ is the fermionic annihilation (creation) operator for the $3d$ state with spin-orbital index $i \in \{\uparrow, \downarrow\}\otimes\{z^2, x^2-y^2, xy, xz, yz\}$. The one-body energy tensor ϵ_d encodes the crystal-field splittings and an atomic spin-orbit coupling interaction with coupling constant ζ_{3d}. For the spectroscopic process, Ni $2p$-$3d$ Coulomb interactions and the core spin-orbit coupling ζ_{2p} are further supplemented. The rotationally invariant Coulomb interaction is parametrized by Slater integrals F^k and G^k [S1]. The ligand L orbitals are treated as non-interacting, and the corresponding term is given as

$$H_L^{t,b} = \sum_i \epsilon_L^{ii}L_i^{\dagger}L_i,$$

where the one-body tensor ϵ_L is diagonal in the absence of spin-orbit coupling of oxygen $2p$ orbitals. Note that we take both ϵ_d and ϵ_L to be traceless, as the mean on-site energies are subject to corrections depending on the Coulomb interaction and charge-transfer energy (see below). The $3d$ orbitals hybridize with their surrounding ligand orbitals as well as the neighboring ones, resulting in intra-cluster (inter-cluster) hybridization terms $V_{dL}^{tt,bb}$ (V_{dL}^{tb}) in the form

$$V_{dL}^{\alpha\beta} = \sum_i t_{dL}^i(d^{\alpha}{}_i^{\dagger}L_i^{\beta} + \text{h.c.}).$$

Similarly, the ligand-ligand hybridization reads

$$V_{LL}^{tb} = \sum_i t_{LL}^i(L^t{}_i^{\dagger}L_i^b + \text{h.c.}).$$

The term $H_{LL'}$ encompasses the one-body terms associated with the remaining ligand orbitals and their coupling to the ligand L orbitals. This term is found to induce minor quantitative changes in the spectral details and holds marginal significance for the ground state properties. Consequently, it will be projected out in the subsequent steps to prevent the introduction of additional parameters.

Parameters. — To minimize bias in parameterization, we estimate the one-body parameters based on values derived from Ni $3d$ and oxygen $2p$ Wannier orbitals constructed through DFT calculations [S2, S3] on the experimental crystal structure of $La_3Ni_2O_7$ under ambient pressure [S4]. The eventual parameters undergo fine-tuning to align with the specifics of the experimental XAS and RIXS spectra, typically converging within 15% of the DFT estimation. The Coulomb Slater integrals are scaled down to 80% of the atomic Hartree-Fock values for Ni^{2+} with $2p^63d^8$ and $2p^53d^9$ configurations for the initial and final states of XAS [S1].

This semi *ab initio* approach leaves three unspecified parameters relevant to the ground-state and spectroscopic properties: the average Coulomb interaction within the $3d$ shell U_{dd}, the interaction between the Ni $2p$ and $3d$ shell U_{pd}, and the charge-transfer energy Δ. Here, Δ is defined as the energy cost of creating a ligand hole in the assumed ground state with fully occupied ligand states, expressed as

$$\Delta = E(d^8d^8\underline{L}) - E(d^7d^8), \tag{S2}$$

where $\underline{L}$ denotes a ligand hole. The above definition relates the mean on-site energies of the $3d$ and ligand orbitals to the Coulomb interaction U_{dd}. For our calculations, we set $U_{dd} = 6.0$ and $U_{pd} = 7.5$ eV, values comparable to those used in previous

	ϵ_d	ϵ_L	$t^{tt/bb}_{dL}$	t^{tb}_{dL}	t^{tb}_{LL}	Other parameters
z^2	0.30	0.30	-2.06	1.02	-0.39	$U_{dd} = 6.00,\ F^2_{dd} = 9.79,\ F^4_{dd} = 6.08$
$x^2 - y^2$	0.36	0.30	-2.80	0.00	0.00	$U_{pd} = 7.50,\ F^2_{pd} = 6.18,\ G^1_{pd} = 4.63,\ G^3_{pd} = 2.63$
xy	-0.27	-0.30	-1.55	0.00	0.00	$\zeta_{3d} = 0.083,\ \zeta_{2p} = 11.50$
xz/yz	-0.18	-0.30	-1.37	0.31	0.20	

TABLE SI. Summary of parameters used for the multiplet calculation, in units of eV. The monopole part of the Coulomb interaction is given as $F^0_{dd} = U_{dd} + \frac{2}{63}(F^2_{dd} + F^4_{dd})$ and $F^0_{pd} = U_{pd} + \frac{1}{15}G^1_{pd} + \frac{3}{70}G^3_{pd}$ for the 3d-3d and 2p-3d interactions, respectively.

studies on perovskite nickelates [S5, S6]. It is important to note that these values should be distinguished from, and are generally larger than, those employed in mean-field-type calculations such as DFT+U in Section 5. Changes within 1 eV do not result in qualitative changes of the ground-state and spectroscopic properties. All the parameters used are summarized in Table SI. The remaining charge-transfer energy Δ is treated as a free parameter and adjusted to fit the experimental XAS spectra, calculated using exact diagonalization as implemented in QUANTY [S7].

2.2 Results.

Charge transfer energy. — Figure S2(a) shows the calculated XAS as a function of Δ. Reasonable agreement with the experiment is achieved for $\Delta \lesssim 1.5$ eV. As Δ further increases, the spectra deviate from the experimental ones, displaying additional peak structures and a noticeable shift between the main peaks with σ and π polarizations. Examination of the ground state configuration in Fig. S2(b) shows that for all the calculated values of Δ, d^8 remains the leading configuration, which contributes to the lowest-energy peak at ~ 852.4 eV in XAS as shown in Fig. S2(c), similar to the case of NiO. For smaller Δ values, the subleading configuration is $d^8\underline{L}$, indicating significant self-doped ligand holes in the ground state. This part of the
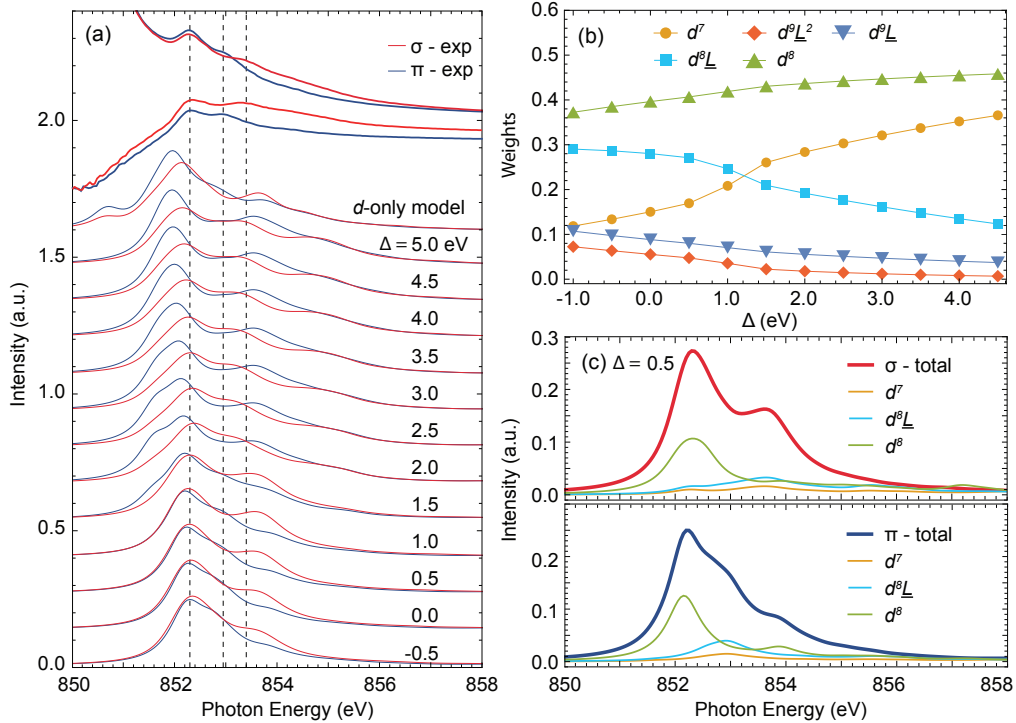

FIG. S2. (a) Calculated XAS with different values of Δ in comparison with the experimental results (both the original XAS spectra and XAS spectra after subtracting signals contributed by the La M_4-edge are appended). The spectra are calculated with an inverse core hole lifetime 0.35 eV and convoluted with a Gaussian function with full width at half maximum (FWHM) 0.20 eV. Typical XAS spectra calculated using a d-only two-site cluster model assuming a $2d^{7.5}$ configuration is also shown for comparison. (b) The ground state electronic configuration projected onto a single NiO$_6$ cluster as a function of Δ. (c) Configuration decomposed XAS for $\Delta = 0.5$ eV. Only the leading contributions are plotted.
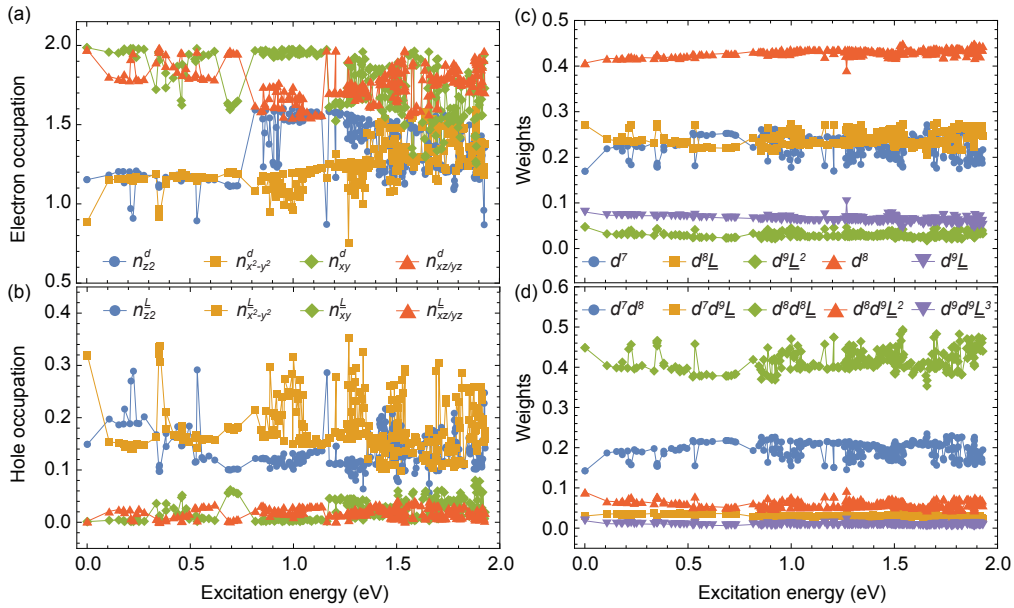
FIG. S3. Characterizations of the excited states up to 2.0 eV. (a,b) Electron and hole occupation of Ni $3d$ and ligand molecular orbitals, respectively. (c,d) Weights of different local and global configurations.

wave function primarily contributes to the high-energy satellite peak in XAS [Fig. S2(c)]. It is worth mentioning here that the full spectral weight does not equal the sum of configuration-decomposed ones, as it also includes interference between different configurations. For $\Delta \gtrsim 1.5$ eV, the weight of d^7 dominates over $d^8\underline{L}$, and the system crossovers to the canonical charge-transfer insulator regime with negligible ligand holes in the ground state, similar to the case of NiO. Note that this crossover also leads to a qualitative change in the XAS line shape, and the agreement between the calculated and experimental XAS progressively deteriorates with further increasing Δ values. For large Δ values, the ground state is well approximated by $\alpha|d^7\rangle + \beta|d^8\rangle$. As shown in Fig. S2(a), the corresponding XAS show similar characteristics to those obtained using a d-only two-site cluster model, integrating out the ligand degrees of freedom and assuming a $2d^{7.5}$ configuration.

The above results highlight the importance of the oxygen degrees of freedom in the electronic structure, and confirm the small-charge-transfer nature in La$_3$Ni$_2$O$_7$. In the following, we will focus on the case of $\Delta = 0.5$ eV, which gives the optimal agreement with the experimental XAS. We note that the results exhibit qualitative consistency across the range of Δ values from 0 to 1.5 eV. Given that the estimated model parameters typically carry an error bar on the order of a fraction of 1 eV, a reasonable conclusion is that $\Delta \lesssim 2$ eV, falling between the values estimated for NiO (~ 5 eV) and RNiO$_3$ (~ 0 eV).

Characterization of the RIXS excitations. — The two sets of RIXS excitations centered around 0.4 eV and 1.0 eV in Fig.1h are well captured in the calculated RIXS spectra. The higher-energy excitation around 1.5 eV is less prominent in calculation. This is partly due to the limited degrees of freedom in the model, which only serve as a crude approximation of the continuum states that give rise to the strong, broad fluorescence background between 0 to 3 eV in experiments. To further understand the nature of these excitations, we characterize the low-energy excited states in the double-cluster model by evaluating their corresponding orbital occupations and wave function configurations.

Figure S3 shows detailed characterizations of the excited states up to 2.0 eV. The excitations observed in RIXS around 0.4 eV involve charge transfers between the orbitals of z^2 and x^2-y^2 symmetry, as indicated by the small decrease of $n_{z^2}^d/n_{z^2}^{\underline{L}}$ and increase of $n_{x^2-y^2}^d/n_{x^2-y^2}^{\underline{L}}$ occupation compared to the ground state in Figs. S3(a) and (b). Further investigation of the states suggests that these excitations are of mixed charge and spin type. The excitations centered around 1 eV involve substantial charge transfers between the d_{z^2} and $d_{xz/yz}$ orbitals, which characterize the crystal-field splitting between the d e_g and t_{2g} orbitals. They involve relatively small movements of the ligand states, signifying almost pure dd-type excitations, similar to those observed in NiO and RNiO$_3$ at a comparable energy. Higher-energy excitations between 1.3~1.5 eV correspond to more complex dd-type excitations, involving transfers between all d orbitals. The excitation energy is somewhat lower than that observed in experiment, potentially owing to the limited in-plane size of the cluster model, which may underrepresent the correlated bandwidth of the planar orbitals. It is noteworthy that these dd excitations overlap in energy with a broad range of charge-transfer excitations between Ni-d and ligand orbitals. This is evident in the fluctuation of wave function configuration weights between the local d^7 and $d^8\underline{L}$ as well as the global d^7d^8 and $d^8d^8\underline{L}$ over almost the entire energy range, as shown in Figs. S3(c) and (d). This is expected for systems with a small charge-transfer energy.
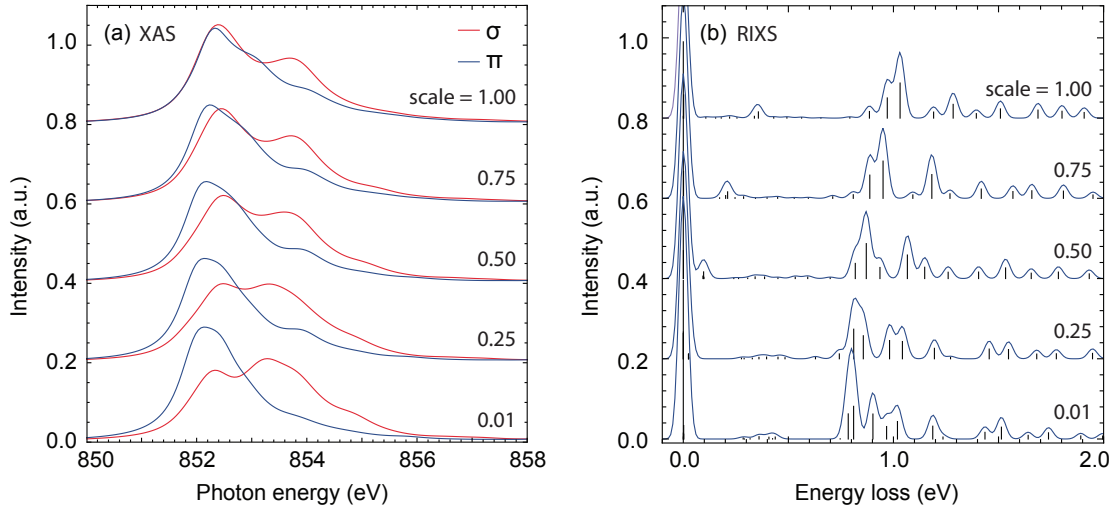
FIG. S4. Calculated (a) XAS and (b) RIXS for V_{dL}^{tb} scaled to 0.01, 0.25, 0.50, and 0.75 of their original values. The spectra calculated with the original values are shown for comparison. The RIXS spectra were obtained by averaging two spectra with π-polarized incident light at, and 0.5 eV above, their corresponding XAS maxima in (a). The discrete poles are convoluted with a Gaussian function of FWHM 0.05 eV to obtain the continuous spectra.
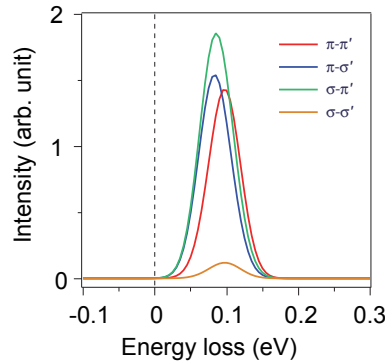

FIG. S5. Calculated polarimetric RIXS decomposed into $\pi - \pi'$, $\pi - \sigma'$, $\sigma - \pi'$, $\sigma - \sigma'$ components. The elastic peak as well as other excitations above 0.2 eV are removed for clarity. The spectra are obtained by convoluting two poles around 0.1 eV with a Gaussion of FWHM 0.05 eV.

Effects of inter-layer coupling. — The importance of explicit consideration of the bilayer geometry for the electronic structure becomes evident upon tuning the inter-layer hoppings V_{dL}^{tb} while keeping all other parameters unchanged. Fig. S4 shows the resultant XAS and RIXS for V_{dL}^{tb} values scaled to different ratios of their original values in Tab. SI. The reduced inter-layer hopping results in a relative energy shift between the XAS with σ and π polarizations in Fig. S4(a). The calculated RIXS excitations are also contingent upon the inter-layer coupling, as illustrated in Fig. S4(b). While the energy of the excitations around 1 eV can be further adjusted by the average e_g-t_{2g} energy splitting in calculation, the excitation around 0.4 eV is more intricately influenced by the inter-layer hopping.

Polarimetric RIXS. — Figure S5 shows the calculated RIXS spectra decomposed into different polarization channels. To obtain spin excitations around 0.1 eV, an exchange field of 0.56 eV is applied along the pseudo-tetragonal *ab* diagonal direction. Compared with other polarization components, the $\sigma - \sigma'$ one contributes negligible spectral weight, as expected for an excitation of magnetic origin.

Supplementary Note 3. Polarisation dependence of magnon excitations at the Ni L_3-edge.

Figure. S6(a) show RIXS intensity plots measured using 852.4 eV π-polarised photons along high-symmetry directions (H,H) and $(H,0)$. The measured dispersion of magnon excitations is consistent with that measured using σ-polarised photons (Fig. 2a in the main text and Fig. S6(b)).
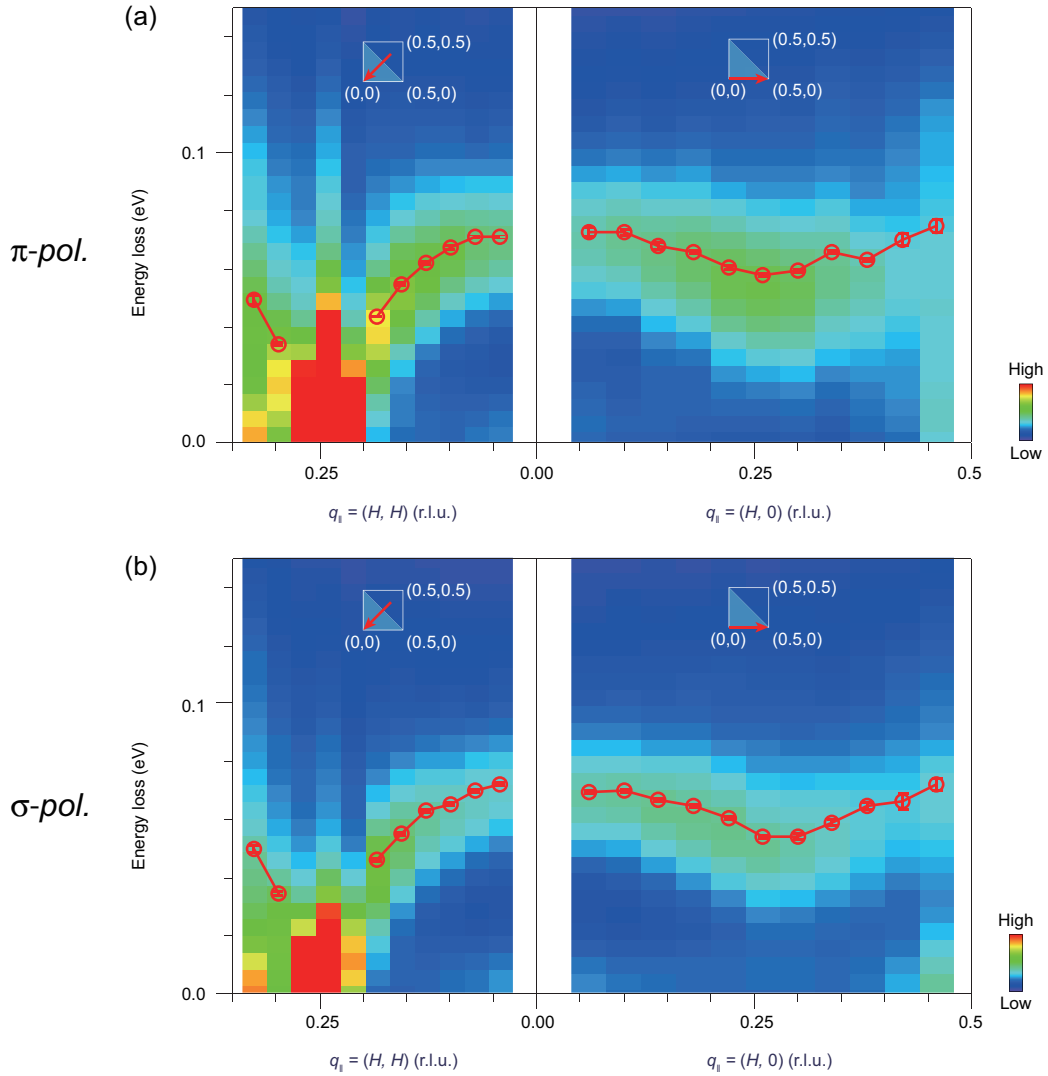

FIG. S6. (a) Magnon excitations measured by π-polarised photons along (H, H) and $(H, 0)$ directions. Data were collected at 20 K using 852.4 eV X-rays at the Ni L_3-edge. (b) Magnon excitations measured by σ-polarised photons along (H, H) and $(H, 0)$ directions. Data were collected at 20 K using 852.4 eV X-rays at the Ni L_3-edge. The magnon peaks were fitted by the damped harmonic oscillator (DHO) function and indicated by the red open circles.

Supplementary Note 4. RIXS data analysis and fitting.

All RIXS data were normalized to the incident photon flux. The positions of elastic peaks were determined from the non-resonant signal of a carbon tape placed near the sample, and subsequently fine-calibrated by fitting the elastic peak to a Gaussian with a fixed full width at half maximum (FWHM) as the instrument resolution (~ 36.5 meV at the Ni L_3 edge). The momentum-dependent RIXS intensities were then corrected for self-absorption effects [S8]. For the final fitting, a constant background was used and the magnon excitations were fitted using the damped harmonic oscillator (DHO) function $\chi''(q, \omega)$, given by

$$\chi''(q, \omega) = \frac{\gamma_q \omega}{(\omega^2 - \varepsilon_q^2)^2 + 4\gamma_q^2 \omega^2}$$

where ε_q is the undamped mode energy, γ_q is the damping factor related to the width of the magnon peak, and ω is the energy loss. The high energy hump ($\gtrsim 0.1$ eV) was also fitted by the DHO function to account for the high-order magnetic excitations (mostly bimagnons) or the high-energy charge background.

Figures S7(a) and S7(b) show two representative Ni L_3-RIXS spectra and corresponding fittings. According to the analysis of polarimetric RIXS results (Fig. 2d in the main text), the low-energy phonon contribution to the RIXS intensity should be negligible, and adding a phonon peak in the fittings does not affect the magnon peak dramatically, as demonstrated in Figs. S7(c) and S7(d). Consequently, the phonon contribution is not considered in the following fittings. Figures S8 and S9 show the fitting results of RIXS spectra displayed in Fig. 2 in the main text.
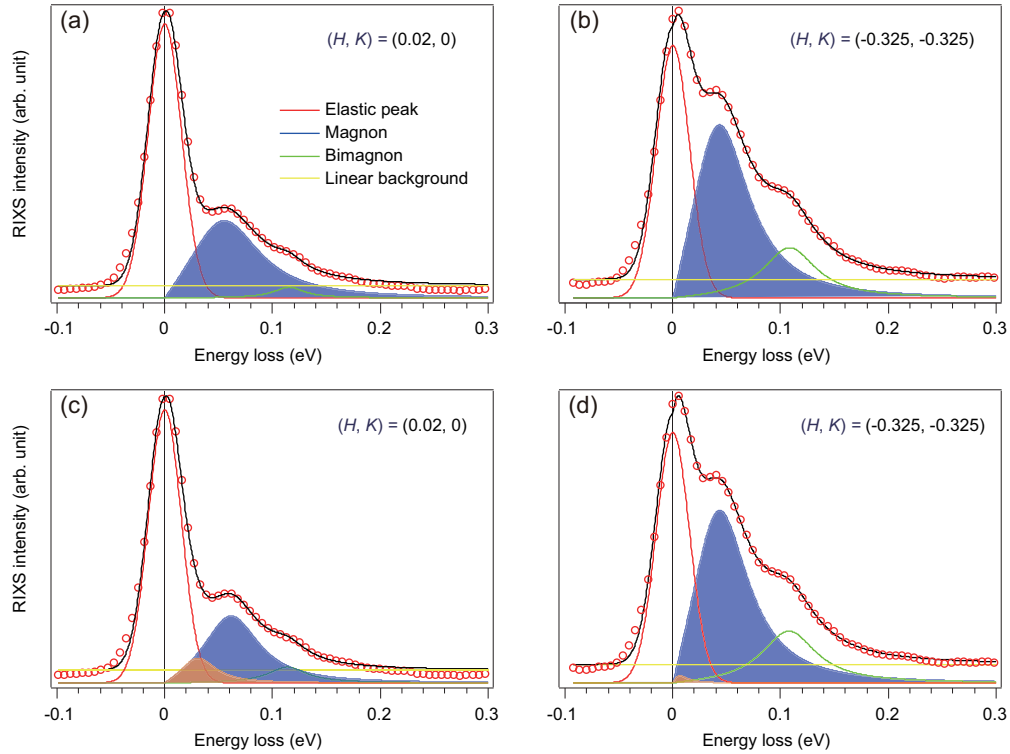

FIG. S7. (a,b) Representative Ni L_3-RIXS spectra measured using σ-polarised, 852.4 eV photons at $(H, K) = (0.02, 0)$ and $(-0.325, -0.325)$, respectively. The corresponding fittings are displayed. The fitted magnon peak is indicated as a blue shade. (c,d) The same Ni L_3-RIXS spectra as displayed in (a,b) while in the fitting a low-energy phonon peak was added (orange shade).
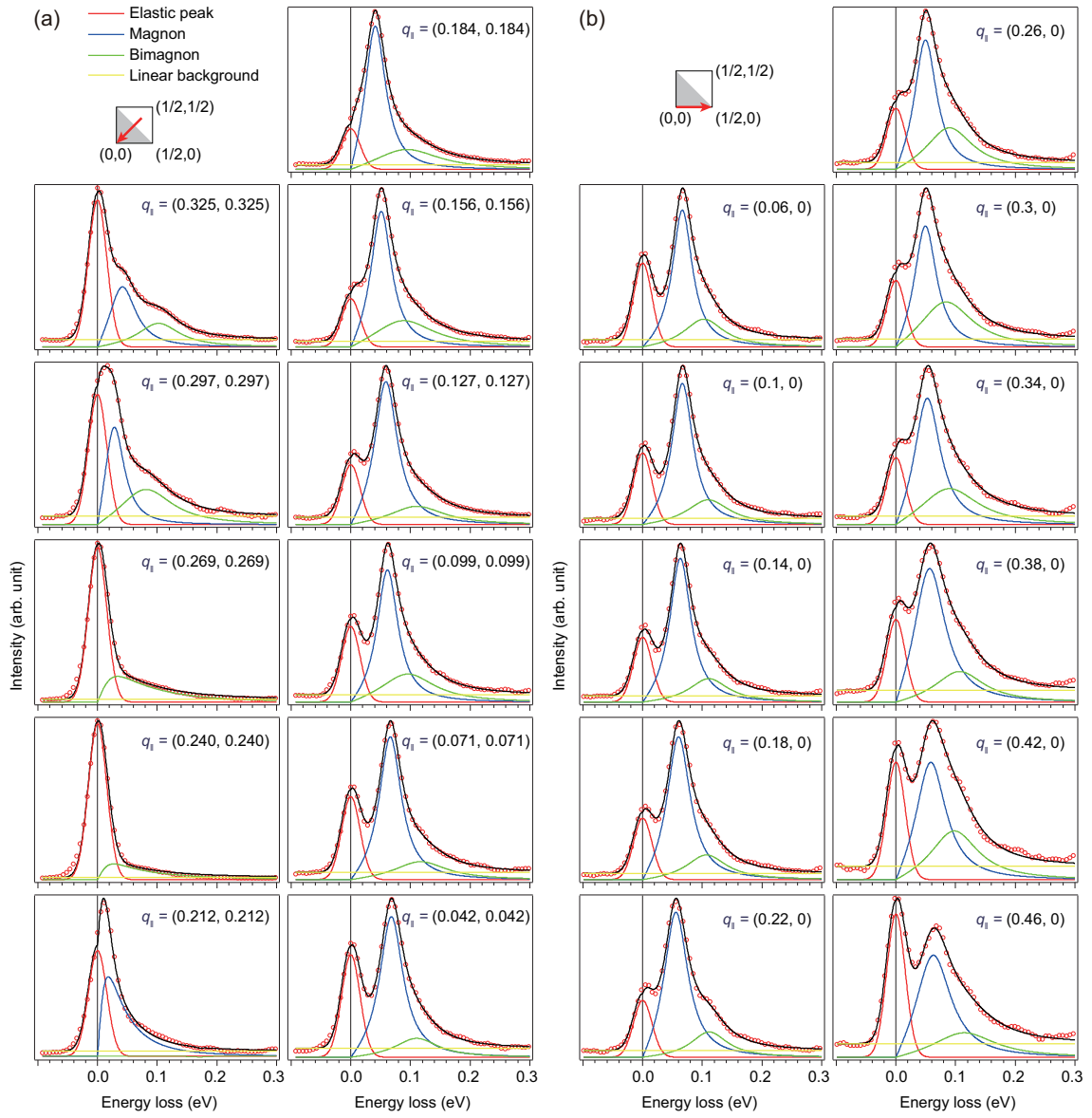
FIG. S8. (a,b) Momentum-dependent RIXS spectra measured using 852.4 eV σ-polarised photons along high-symmetry directions (H, H) and $(H, 0)$, respectively. The corresponding fitting results are appended. The elastic peak is fitted by a Gaussian. The magnon and bimagnon are fitted by the damped harmonic oscillator (DHO) function.

FIG. S9. (a,b) Momentum-dependent RIXS spectra measured using 852.4 eV σ-polarised photons along high-symmetry directions (H, 0.5-H) and (0.25, K), respectively. The corresponding fitting results are appended. The elastic peak is fitted by a Gaussian. The magnon and bimagnon are fitted by the damped harmonic oscillator (DHO) function.
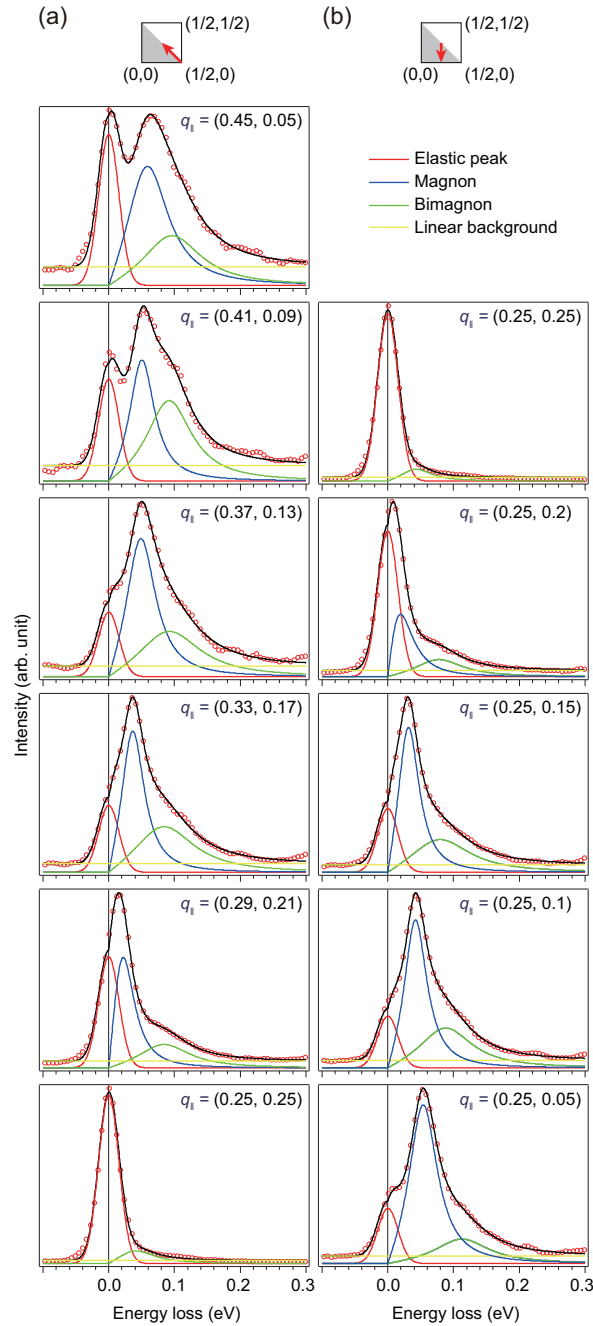
Supplementary Note 5. DFT computational method and spin order.

In order to explore possible spin density wave (SDW) orders, we perform a density functional theory (DFT) calculation. Our DFT calculations employ the Vienna ab-initio simulation package (VASP) code [S9] with the projector augmented wave (PAW) method [S10]. The Perdew-Burke-Ernzerhof (PBE) exchange-correlation functional [S11] is used. The energy cutoff energy for expanding the wave functions into a plane-wave basis is set to be 500 eV. The experimental crystal structure is used in the calculation. The Γ-centered k-mesh is used in KPOINTS files which are generated by VASPKIT [S12] with the KPT-resolved value equal to 0.02 for different unit cells. The SDW orders are calculated using the simplified rotation invariant approach based on the DFT+U method introduced by Dudarev *et al*. [S13]. Since the RIXS has identified the $Q_{SDW} = (0.25, 0.25)$ or $(\pi/2, \pi/2)$ spin pattern, we will focus on the possible Q stripe order. Three SDW patterns are listed in Figs. S11(a-c). The first

pattern is the spin-charge intertwined stripe order (Stripe-1) as illustrated in Fig. S11(a), which has been observed in half-doped $La_{3/2}Sr_{1/2}NiO_4$ [S14]. We use up/down arrows to represent spin up/down sites, and black balls for charge sites. Owing to the strong bilayer bonding, the spins are also flipped between the top and bottom Ni layers [S4, S14]. One can also exchange the charge chain positions to arrive at the double spin-charge stripe (Stripe-3), as illustrated in Fig. S11(c). The third SDW order is the double spin stripe order (Stripe-2) without charge order, as illustrated in Fig. S11(b). This Stripe-2 order is similar to the collinear double-stripe state discovered in FeTe [S15]. Based on DFT+U calculation, the ground state energies for the above three spin configurations and the G-type AFM (ordering at (π, π)) are listed in Table. SII. The Stripe-2 order is found to be the lowest energy state up to U=4.0 eV while the stripe-1 order is just slightly lower in energy.

TABLE SII. Total energy (in units eV) per Ni atom of the different magnetic configurations.

	$U = 0$	$U = 1$	$U = 2$	$U = 3$	$U = 4$
Stripe-1	-179.335	-177.312	-175.485	-173.82	-172.217
Stripe-2	-179.386	-177.493	-175.797	-174.269	-172.897
Stripe-3	-179.298	-177.31	-175.536	-173.931	-172.071
G-AFM	-179.306	-177.3	-175.489	-173.852	-172.39

The calculated magnetic moments are listed in Table SIII. Although there are non-magnetic sites (black in Fig.S10(c)) for the initial inputs, the pure charge sites develop small non-zero values after self-consistent calculation for $U > 0$. Therefore, we list them by the slash line in Table SIII. The majority spin moment competes with the minority spin moment in the large U leading to a decreased minority spin moment in $U = 4$. Hence, there is an obvious energy change in $U = 4$. We also want to emphasize that DFT+U always overestimates the magnetic moments, and the limited supercell size makes it challenging to capture the spin-density-wave nature in the current DFT calculations. Nevertheless, the metallic band structure from current DFT results (Fig. S10) and the ordering tendency at $Q = (\pi/2, \pi/2)$ align well with the RIXS observations. Experimentally, the studies of the magnetic moment show some contradictory results. NMR estimates that the magnetic moments at Ni sites are $\sim 0.08\ \mu_B$ for Ni with inner apical oxygen and $0.018\ \mu_B$ for Ni without inner apical oxygen [S16]. The recent μSR work estimates that the magnetic moment is 0.48-0.67 μ_B if the moment points in the ab-plane, while 0.28-0.31 μ_B if the moment points parallel to the c-axis [S17].

TABLE SIII. The calculated magnetic moments (in units μ_B) at Ni sites for different magnetic configurations.

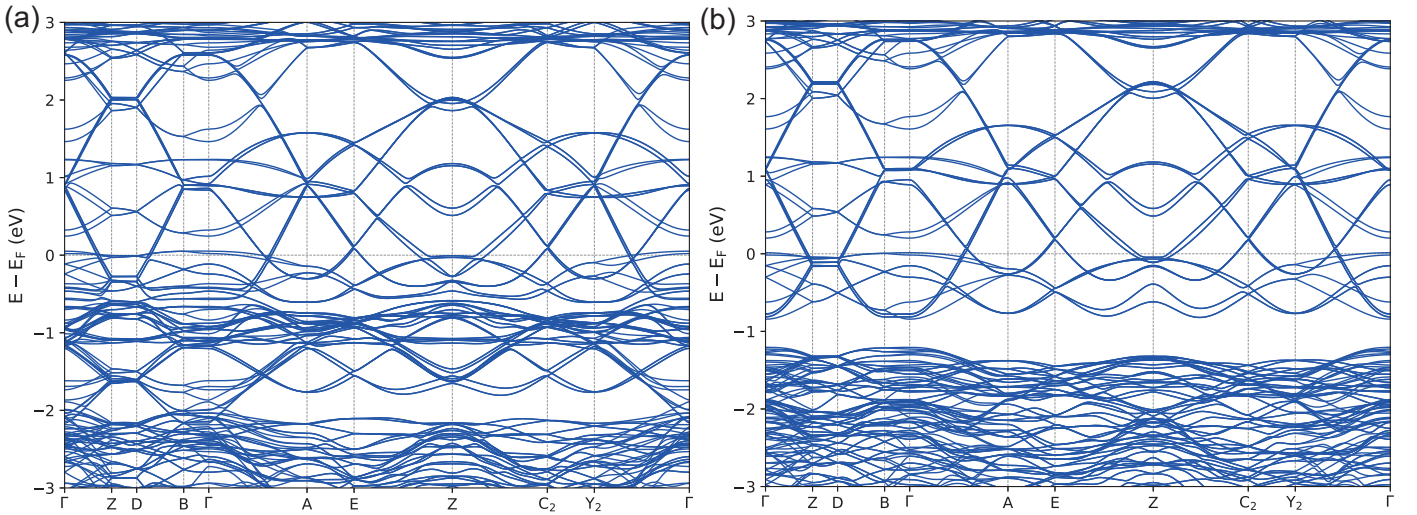|	$U = 0$	$U = 1$	$U = 2$	$U = 3$	$U = 4$
Stripe-1	0.806	1.08	1.264	1.374	1.493
Stripe-2	0.716	0.941	1.076	1.185	1.282
Stripe-3	0.699/0.0	0.971/0.444	1.163/0.459	1.294/0.473	1.379/0.338
G-AFM	0.517	0.748	0.917	1.061	1.194

FIG. S10. The band structures of Stripe-2 configuration or E-type AFM from DFT+U calculations. (a) $U = 0$ eV. (b) $U = 4$ eV.

Supplementary Note 6. Magnetic excitations in the stripe-order states.

In this section, we compute the spin dynamics dispersion relations for the above stripe states. We want to emphasize that the system we consider here is a spin-density wave. Formally, we can write down a semiclassical equation for its spin dynamics [S18]

$$\frac{\partial S_i}{\partial t} = -S_i \times \frac{\langle \hat{H}_{SDW} \rangle}{\partial S_i} \tag{S3}$$

where $\hat{H}_{SDW}$ is the full Hamiltonian of the SDW orders. However, since the $\hat{H}_{SDW}$ dynamics is complicated with two-layer, 4-sites, and 2-orbital model, we replace the $\hat{H}_{SDW}$ by the effective Heisenberg model of the spin degree of freedom for simplicity and leave the full consideration for future. The couplings J should be considered as the Weiss molecular field. We consider three models with the effective Heisenberg interactions illustrated in Fig. S11(a-c) to reproduce the observed magnon dispersion in the experiments. J_1 and J_2 are the in-plane couplings where J_1 couples nearest-neighbor spins and J_2 couples the next nearest-neighbor spins. J_z couples spins between layers within the bilayer in the [0, 0, 1] direction. The Hamiltonians can be written as

$$H = \sum_i J_z \vec{S}_i^t \cdot \vec{S}_i^b + \sum_{\langle ij \rangle \alpha} J_1 \vec{S}_i^\alpha \cdot \vec{S}_j^\alpha + \sum_{\langle\langle ij \rangle\rangle \alpha} J_2 \vec{S}_i^\alpha \cdot \vec{S}_j^\alpha \tag{S4}$$

where the α is the layer index for the bottom (b) or top (t) layer. $\langle ij \rangle$ and $\langle\langle ij \rangle\rangle$ are the nearest-neighbor and next nearest-neighbor defined in Fig. S11(a-c) for each spin configuration.

The in-plane lattice vectors for the structural unit cell are

$$\boldsymbol{a}_1 = (a, 0, 0), \quad \boldsymbol{a}_2 = (0, a, 0) \tag{S5}$$

and for all three stripe configurations, the lattice vectors of the magnetic unit cell are

$$\boldsymbol{a}_1^{mag} = (4a, 0, 0), \quad \boldsymbol{a}_2^{mag} = (-a, a, 0). \tag{S6}$$

The reciprocal lattice vectors for this magnetic primitive unit cell are

$$\boldsymbol{b}_1^{mag} = \frac{2\pi}{a} \left(\frac{1}{4}, \frac{1}{4}, 0 \right), \quad \boldsymbol{b}_2^{mag} = \frac{2\pi}{a} (0, 1, 0), \tag{S7}$$

which indicates that the magnon dispersion becomes gapless at point $\left(\frac{\pi}{2}, \frac{\pi}{2} \right)$.

We calculate the magnon dispersion within the linear spin wave theory and use the torque equation formalism[S19, S20] (which is equivalent to the Holstein-Primakoff treatment at the lowest order). As in our cases, the spins in the ground state are oriented along c, the torque equations for the spins reduce to

$$\frac{dS_{\boldsymbol{r},i}^x}{dt} = -\frac{1}{\hbar} \left(S_{\boldsymbol{r},i}^y \sum_{\boldsymbol{r}',j} J_{\boldsymbol{rr}'}^{ij} S_{\boldsymbol{r}',j}^z - S_{\boldsymbol{r},i}^z \sum_{\boldsymbol{r}',j} J_{\boldsymbol{rr}'}^{ij} S_{\boldsymbol{r}',j}^y \right),$$

$$\frac{dS_{\boldsymbol{r},i}^y}{dt} = -\frac{1}{\hbar} \left(S_{\boldsymbol{r},i}^z \sum_{\boldsymbol{r}',j} J_{\boldsymbol{rr}'}^{ij} S_{\boldsymbol{r}',j}^x - S_{\boldsymbol{r},i}^x \sum_{\boldsymbol{r}',j} J_{\boldsymbol{rr}'}^{ij} S_{\boldsymbol{r}',j}^z \right), \tag{S8}$$

$$\frac{dS_{\boldsymbol{r},i}^z}{dt} \approx 0,$$

where $\boldsymbol{r}, \boldsymbol{r}'$ label the positions of the spins in different magnetic unit cells and the indices i, j label the spins within each magnetic unit cell. We seek the plane-wave like solutions of the form

$$S_{\boldsymbol{r},i}^x = S_i^x \exp[i\boldsymbol{Q} \cdot \boldsymbol{r} - i\omega t], \quad S_{\boldsymbol{r},i}^y = S_i^y \exp[i\boldsymbol{Q} \cdot \boldsymbol{r} - i\omega t] \tag{S9}$$

and we set $S_{\boldsymbol{r},i}^z = \pm S$ with the sign given by the orientation of the spin in the ground state. Using Eq. (S8) and Eq. (S9), we can obtain the eigen equation for the magnon dispersion $\omega(\boldsymbol{Q})$. We denote the orthogonal eigenvectors as $v_{n,\boldsymbol{Q}} = \left(c_{n,\boldsymbol{Q},1}^x, c_{n,\boldsymbol{Q},1}^y, ..., c_{n,\boldsymbol{Q},i}^x, c_{n,\boldsymbol{Q},i}^y, ... \right)$, where n denotes the n-th eigenvector and index i denotes the i-th spin in a magnetic unit cell. Therefore for the n-th magnon mode, its magnetization vector at site i is $M_{n,\boldsymbol{Q}}(\boldsymbol{r}_i) = S \left(c_{n,\boldsymbol{Q},i}^x, c_{n,\boldsymbol{Q},i}^y, 0 \right)$. The RIXS intensity for the n-th magnon mode in the σ-π polarisation channel is given by Ref. [S20]

$$I_n(\boldsymbol{Q}) = \sum_i \left| \boldsymbol{k}_{out} \cdot M_{n,\boldsymbol{Q}}(\boldsymbol{r}_i) \right|^2, \tag{S10}$$

	Stripe-1	Stripe-2	Stripe-3
J_1S (meV)	3.55 ± 0.04	0.00 ± 0.10	10.56 ± 0.15
J_2S (meV)	2.01 ± 0.01	4.13 ± 0.04	7.11 ± 0.05
J_zS (meV)	67.18 ± 0.89	73.89 ± 0.71	25.99 ± 0.29

TABLE SIV. The fitting parameters of different models in Fig. S11.

where $\boldsymbol{k}_{out}$ is the outgoing wave vector. The scattering angle $2\theta = 154°$ is fixed during the experiments, therefore the transferred momentum can be determined by

$$|\boldsymbol{Q}| = \frac{4\pi \sin\theta}{\lambda_E}, \tag{S11}$$

where λ_E is the photon wavelength. The outgoing wave vector can be calculated as

$$\boldsymbol{k}_{out} = \cos\theta \boldsymbol{I} + \sin\theta \boldsymbol{Q}, \tag{S12}$$

with $\boldsymbol{I} = \frac{\boldsymbol{Q} \times \boldsymbol{c} \times \boldsymbol{Q}}{|\boldsymbol{c} \times \boldsymbol{Q}|}$. We note that as the in-plane component of $\boldsymbol{Q}$ is swept, the Q_z component changes accordingly, which plays an essential role in the varying of intensities of different magnon modes. We use intensity $I_n(\boldsymbol{Q})$ as the weight to perform weighted averaging on $\omega_n(\boldsymbol{Q})$ and take the weighted averaged $\bar{\omega}(\boldsymbol{Q})$ to fit the experimental data. The results are shown in Fig. S11(d-f), where the black dots are the experimental data and solid lines are the fitting curves.

From Fig. S11(d-e), we can see the Stripe-1 and Stripe-2 models fit the experimental data well. The intensities for acoustic spin dispersion are quite weak owing to the X-ray scattering matrix. We summarize the fitting parameters for different models in Table. SIV. All three models have relatively strong interlayer effective couplings J_zS. On the other hand, the J_1 coupling in Stripe-2 is relatively weak. Therefore, the spin dynamic equations in Stripe-2 are similar to Stripe-1, resulting in similar magnon dispersions. The mixture of Stripe-1 and Stripe-2 also has similar magnon dynamics. Here all calculations are performed based on single-domain configurations, without considering the effects of twinning.
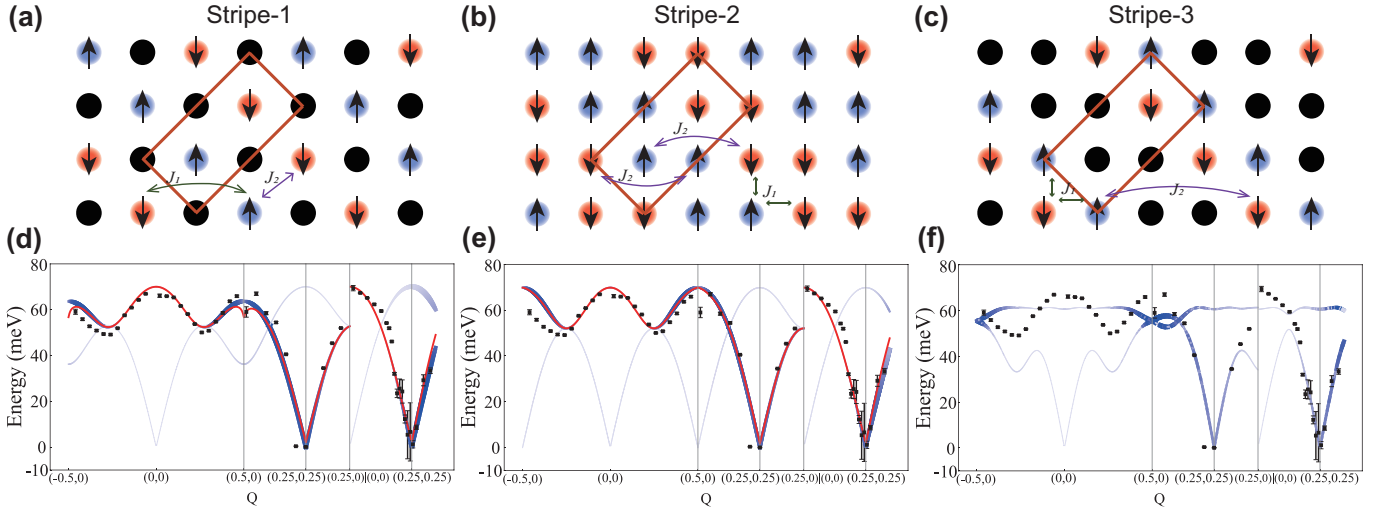

FIG. S11. (a)-(c) The schematic illustration for the three considered $(\pi/2, \pi/2)$ stripe spin order in La$_3$Ni$_2$O$_7$ lattice. Here, we only plot the top layer while the spins are flipped at the bottom layer. The blue, red, and black filled circles represent spin up, spin down, and charge sites, respectively. The brown lines represent the primitive magnetic unit cell in a plane, respectively. (a) The stripe-1 order. (b) The stripe-2 order. (c) The stripe-3 order. (d)-(f) The fitting of the three models in (a)-(c). The blue lines are the dispersion relations of different magnon modes, where the thicknesses of the lines and the depth of their color represent the intensity of the modes. The red lines are the weighted averaged magnon dispersion $\bar{\omega}(\boldsymbol{Q})$. Since in case (f) the intensity of the modes varies dramatically with $\boldsymbol{Q}$ leading to a strongly oscillated weighted averaged dispersion, we do not present $\bar{\omega}(\boldsymbol{Q})$ in this case. In cases (d) and (f), each magnon mode is doubly degenerate. For case (e), each mode has quadruple degeneracy.

[S1] Cowan, R. D. *The Theory of Atomic Structure and Spectra* (Univ of California Press, 1981).

[S2] Blaha, P. *et al.* WIEN2k: An APW+lo program for calculating the properties of solids. *J. Chem. Phys.* **152**, 074101 (2020).

[S3] Pizzi, G. *et al.* Wannier90 as a community code: new features and applications. *J. Phys. Condens. Matter* **32**, 165902 (2020).

[S4] Sun, H. *et al.* Signatures of superconductivity near 80 K in a nickelate under high pressure. *Nature* **621**, 493–498 (2023).

[S5] Green, R. J., Haverkort, M. W. & Sawatzky, G. A. Bond disproportionation and dynamical charge fluctuations in the perovskite rare-earth nickelates. *Phys. Rev. B* **94**, 195127 (2016).

[S6] Lu, Y. *et al.* Site-selective probe of magnetic excitations in rare-earth nickelates using resonant inelastic X-ray scattering. *Phys. Rev. X* **8**, 031014 (2018).

[S7] Haverkort, M. W. Quanty for core level spectroscopy - excitons, resonances and band excitations in time and frequency domain. *J. Phys. Conf. Ser.* **712**, 012001 (2016).

[S8] Robarts, H. C. *et al.* Dynamical spin susceptibility in La_2CuO_4 studied by resonant inelastic X-ray scattering. *Phys. Rev. B* **103**, 224427 (2021).

[S9] Kresse, G. & Furthmüller, J. Efficient iterative schemes for ab initio total-energy calculations using a plane-wave basis set. *Phys. Rev. B* **54**, 11169 (1996).

[S10] Kresse, G. & Joubert, D. From ultrasoft pseudopotentials to the projector augmented-wave method. *Phys. Rev. B* **59**, 1758 (1999).

[S11] Perdew, J. P., Burke, K. & Ernzerhof, M. Generalized gradient approximation made simple. *Phys. Rev. Lett.* **77**, 3865 (1996).

[S12] Wang, V., Xu, N., Liu, J.-C., Tang, G. & Geng, W.-T. Vaspkit: A user-friendly interface facilitating high-throughput computing and analysis using vasp code. *Computer Physics Communications* **267**, 108033 (2021).

[S13] Dudarev, S. L., Botton, G. A., Savrasov, S. Y., Humphreys, C. & Sutton, A. P. Electron-energy-loss spectra and the structural stability of nickel oxide: An LSDA+ U study. *Phys. Rev. B* **57**, 1505 (1998).

[S14] Freeman, P. *et al.* Spin dynamics of half-doped $La_{3/2}Sr_{1/2}NiO_4$. *Phys. Rev. B* **71**, 174412 (2005).

[S15] Lipscombe, O. J. *et al.* Spin waves in the (π,0) magnetically ordered iron chalcogenide $Fe_{1.05}Te$. *Phys. Rev. Lett.* **106**, 057004 (2011).

[S16] Dan, Z. *et al.* Spin-density-wave transition in double-layer nickelate $La_3Ni_2O_7$. *arXiv preprint arXiv:2402.03952* (2024).

[S17] Khasanov, R. *et al.* Pressure-Induced Split of the Density Wave Transitions in $La_3Ni_2O_{7-\delta}$. *arXiv preprint arXiv:2402.10485* (2024).

[S18] Chern, G.-W., Barros, K., Wang, Z., Suwa, H. & Batista, C. D. Semiclassical dynamics of spin density waves. *Physical Review B* **97**, 035120 (2018).

[S19] Carlson, E. W., Yao, D. X. & Campbell, D. K. Spin waves in striped phases. *Phys. Rev. B* **70**, 064505 (2004).

[S20] Lin, J. *et al.* Strong superexchange in a $d^{9-\delta}$ nickelate revealed by resonant inelastic X-ray scattering. *Phys. Rev. Lett.* **126**, 087001 (2021).